Surface topography and cross-section analysis of K340 cold work tool steel double-tracks deposited by directed energy deposition technique

Original
Surface topography and cross-section analysis of K340 cold work tool steel double-tracks deposited by directed energy deposition technique / Kenevisi, M.S., Gobber, F.S., Maculotti, G., Genta, G., Galetto, M., Biamino, S., Ugues, D.. - In: CIRP - JOURNAL OF MANUFACTURING SCIENCE AND TECHNOLOGY. - ISSN 1755-5817. - 59:(2025), pp. 158-169. [10.1016/j.cirpj.2025.03.011]

Availability:
This version is available at: 11583/2998902 since: 2025-04-07T08:26:09Z

Publisher:
Elsevier

Published
DOI:10.1016/j.cirpj.2025.03.011

CIRP Journal of Manufacturing Science and Technology 59 (2025) 158–169

Contents lists available at ScienceDirect

CIRP Journal of Manufacturing Science and Technology

journal homepage: www.elsevier.com/locate/cirpj

Surface topography and cross-section analysis of K340 cold work tool steel double-tracks deposited by directed energy deposition technique

Mohammad Saleh Kenevisi [a,b,*], Federico Simone Gobber [a], Giacomo Maculotti [c,d], Gianfranco Genta [c,d], Maurizio Galetto [c,d], Sara Biamino [a,b,e], Daniele Ugues [a,b,e]

[a] *Department of Applied Science and Technology (DISAT), Politecnico di Torino, Italy*
[b] *Integrated Additive Manufacturing iAM@PoliTO Center, Politecnico di Torino, Italy*
[c] *Department of Management and Production Engineering (DIGEP), Politecnico di Torino, Italy*
[d] *Manufacturing Industry 4.0 Laboratory (Mind4Lab), Politecnico di Torino, Italy*
[e] *National Interuniversity Consortium of Materials Science and Technology (INSTM), Italy*

ARTICLE INFO

Keywords:
Directed energy deposition
Additive manufacturing
Tool steel
Topography
Design of experiments

ABSTRACT

Tool steels are widely used as dies and tools due to their exceptional properties. However, cracking and wear can significantly impact the performance and longevity of the tools. The possibility of repairing the damaged parts by Directed Energy Deposition (DED) results in an extended tool life and improved environmental impact compared to traditional techniques. To this purpose, the current study aims at investigating the processability of K340 cold work steel by DED. To study the processing window, based on a face-centered composite design, double-tracks with different sets of nozzle travel speed (v_N), laser power (P), and carrier gas flow rate (V_{cg}) were deposited. Deposits were characterized by scanning electron microscopy (SEM), coherence scanning interferometry (CSI), and micro-instrumented indentation, and quantitative analysis of influence factors was performed by ANOVA and response surface methodology. The results showed that increasing P and decreasing v_N resulted in an improved surface roughness. However, surface features describing extreme values, such as Sp and Sz, showed the presence of not fully incorporated particles. Additionally, V_{cg} showed no significant effect on parameters describing the average roughness, such as Sa, Sq and Sdq. Cross-section analysis revealed that almost defect-free deposits can be made with a porosity fraction area of as low as 0.04 %. However, the deposited material showed a different microstructure than that of the substrate, and heat affected zones were also observed. By increasing P, the dilution tended to rise from 5 % to 36 %. The laser power was shown to be the main parameter affecting the dilution. The process optimization to have the best possible combination of high geometrical accuracy and low surface roughness and low defect level was implemented and validated by experimental results. By investigating the processing window and optimizing the process, this study facilitates the application of DED as a repairing process of K340 tools and contributes to sustainable manufacturing.

1. Introduction

Directed energy deposition (DED) is a metal additive manufacturing (AM) technique, in which a focused energy source is used to precisely deposit material during the process to repair parts or create complicated metal components [1]. In comparison to conventional manufacturing techniques, the use of DED has a number of benefits, such as the ability to repair damaged or worn-out components, optimize designs for improved performance, and shorten lead times [2,3]. In the literature, the DED process has been analyzed in-depth in different aspects such as the equipment and nozzle design [4,5], process in-situ monitoring [6], processability of different alloys [7–10], and modeling [11].

Like in each AM technique, the DED processing parameters play an important role in determining the morphology and surface properties of the component, final microstructure of the alloy, and defects formation. Chen et al. [12] investigated the effect of energy density on the process and microstructure of the 18Ni300 maraging steel and reported dilution values of as high as 75 % at high energy densities, which is normally considered as unnecessary high values. In DED process, powder feed, shielding gas, and carrier gas flow rates as well as the atmosphere

---

[*] Corresponding author at: Department of Applied Science and Technology (DISAT), Politecnico di Torino, Italy.
E-mail address: saleh.kenevisi@polito.it (M.S. Kenevisi).

https://doi.org/10.1016/j.cirpj.2025.03.011
Received 3 November 2024; Received in revised form 11 March 2025; Accepted 26 March 2025
Available online 2 April 2025

around the melt pool are important factors that affect the morphology and microstructure of the deposits. Research has demonstrated that increasing the shielding gas flow rate from 5 to 25 l/min can reduce the oxygen content in 316 L parts by nearly 50 % [13]. The carrier gas, responsible for transferring powder particles from the hopper to the nozzle, must also be carefully managed. Excessive increases in carrier gas flow rate can reduce process efficiency by altering the focal point of the powder flow [14].

In terms of surface finishing, it is reported that the average roughness *Ra* of the components fabricated by DED is within the range of 8 to 35 μm [15,16]. One of the approaches to improve the surface roughness is remelting, practice for which the surface is scanned without feeding any powder [17]. Additionally, Cao et al. [18] tried to optimize the surface roughness and dimensional accuracy by proposing a machine learning framework by integrating a gaussian process regression model.

While surface quality is essential in AM processes, material selection also plays a vital role in achieving desired performance characteristics. For instance, K340 alloy, a high-performance cold-work tool steel primarily composed of carbon, chromium, molybdenum, and vanadium, stands out for its exceptional properties. Its microstructure, characterized by fine carbides evenly distributed throughout the matrix, makes it particularly well-suited for cold work applications, such as stamping dies, where high hardness, toughness, and wear resistance are crucial [19]. However, despite its impressive qualities, dies used in blanking or fine blanking processes are vulnerable to various forms of wear, deterioration, and development of cracks over time. The occurrence of defects in fine blanking dies can greatly undermine the efficiency and durability of the entire manufacturing procedure and affect productivity and total operational expenses. To tackle these problems, novel methods for repairing have arisen, and one particularly advanced technology is DED. This technology has clear benefits, such as accurate material deposition and minimal heat affected zone. Several works have been carried out to study and enhance the capability of the DED technique for repairing purposes of different materials such as steels [20], Ti [21], and Ni [22] alloys. However, processing tool steels by AM processes is considered challenging and lots of defects, such as cracks, can be formed [23,24]. This is generally attributed to the high solidification rates, segregation and evaporation, and the melt pool dynamics.

To the best knowledge of the authors, the possibility of applying DED process for repairing K340 tool steel parts has not been investigated yet. The very first step of studying the processability of any new material with an additive manufacturing process is single-layer deposition, normally single-tracks. Implementing single-layer tests can effectively minimize the need for doing multiple layer experiments in order to determine the optimal process parameters and investigating the processing window [2,25,26].

Traditionally, the process window of an alloy is studied by investigating the effect of processing parameters on the deposits one variable at a time (OVAT) approach. However, by applying a Design of Experiments (DoE) approach, the effect of processing parameters can be assessed simultaneously, where the interactions of the selected parameters are also considered. This makes the process optimization more accurate [27]. Surface response methodology and ANOVA [28], Taguchi experiment [29], and Taguchi-Grey relational analysis [30] have been used to optimize the porosity, surface quality, and deposition rate of the process. Nevertheless, in the literature, the optimization is mainly focused on individual quality control variable, such as surface quality or internal defects, whilst there is a need to perform the analysis and optimization considering multiple quality control variables at once, where there might be some conflicting quality responses as well [31–33].

The novelty of this study lies in its systematic investigation of the processability of K340 cold work tool steel via DED — a material and approach combination that, to the best knowledge of the authors, have not been previously reported. By employing DoE technique and a face-centered composite design, this work not only analyzes the influence of key processing parameters on the beads geometrical and topographical properties and internal defects but also integrates a multi-response optimization framework by using a weighted and bounded parametric optimization for composite desirability, i.e. Desirability Optimization Methodology [34]. This comprehensive approach enables a more accurate prediction of deposit quality and is particularly relevant for repair applications in tool manufacturing, thereby advancing sustainable production practices. In the current work, investigations were conducted on double-track depositions.

2. Materials and methods

The K340 alloy powder is not commercially available. Therefore, to produce the feedstock material for this study, K340 scrap from industrial production was used. The scrap was loaded in a Hermiga 100/10 VI gas atomizer, manufactured by PSI Ltd and installed at Politecnico di Torino, where it was atomized using argon gas to produce the necessary powders. The production was then sieved to get a powder with the nominal particle size ranging from 45 to 125 μm. In more detail, the D10, D50, and D90 of the supplied powder were 53.9, 87.8, and 139.6 μm, respectively. The particle size distribution (PSD), and the micrographs of the powder particles and the particle's cross-sections are illustrated in Fig. 1.

As can be seen in Fig. 1b, powder particles are generally spherical-shaped, and a few numbers of satellites attached to the particles is observed. Moreover, cross-section investigation of the particles proved that the presence of the internal gas pores is not significant, as shown in Fig. 1c.

The chemical composition of the powder was studied by using a Zeiss EVO 15 scanning electron microscope (SEM) equipped with an Ultim Max EDS detector by Oxford Instruments. To obtain an accurate analysis, the carbon, oxygen, and sulfur contents were analyzed by LECO ONH836 and CS844 instruments. The results for the main elements are provided in Table 1. Additionally, the sulfur content was negligible, and the oxygen content was 123 ppm.

A K340 plate with the size of 80 × 80 × 10 mm was used as the substrate and was sandblasted prior to deposition. This is beneficial in terms of reducing the reflection of the laser beam and cleaning the surface from any contamination.

The DED process was performed by a Laserdyne 430 laser metal deposition machine at IAM@Polito produced by Prima Additive Co. The machine is equipped with a 1 kW Yb laser and a coaxial powder nozzle. Fig. 2 schematically illustrates the double track depositions. Depositing double-tracks instead of the traditional single-track deposition allows investigating the effect of overlapping on the final height of the track and the possible formation of lack of fusions between two adjacent tracks [35].

The chamber was protected by Argon during the deposition process to avoid oxidation of the material. In this study, the effect of three processing parameters, namely laser power, nozzle speed, and carrier gas flow rate, was studied and the values of the processing parameters were chosen based on the DoE method. A face-centered central composite design was used in this work [36]. The ranges were selected according to the literature and preliminary investigations, and the details of the processing parameters are listed in Table 2.

The other parameters were kept constant and were chosen based on preliminary experimental results. The overlapping between the two tracks was 60 % and the powder feed rate was also maintained at 6 g/min. In total, fifteen depositions with different sets of processing parameters with the length of 15 mm were deposited. The samples were then cut, and the topography of the depositions was studied by Leica DMI 5000 Mlight optical microscope (LOM) and coherence scanning interferometry (CSI) using a Zygo NewView9000 equipment, hosted in the metrological room of the Mind4Lab at DIGEP-Politecnico di Torino. The CSI was used to measure the surface topography of the deposited tracks, by means of a 20 × magnification Mirau objective with digital zoom of 0.5 × (NA 0.4, Field of View (FoV) of (0.87 ×0.87) mm with

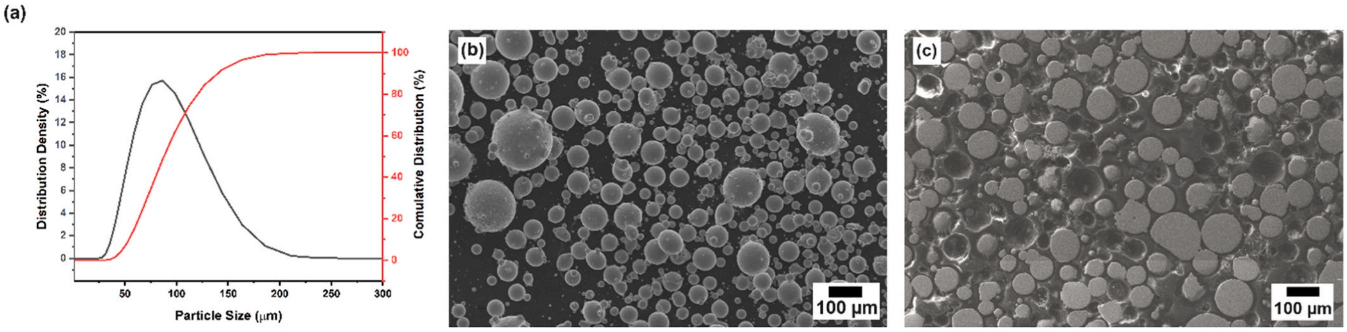

Fig. 1. – a) PSD of the powder, b) SEM micrographs of the particles, and c) the cross-section of the powder particles.

Table 1
Chemical composition (wt%) of the atomized powder used in this study (The exact values of Al and Nb are not stated by the alloy producer).

Element	C	Cr	Mo	V	Si	Mn	Nb	Al
Powder	1.12	8.05	1.91	0.42	0.81	0.46	0.16	0.89
Nominal	1.10	8.30	2.10	0.50	0.90	0.40	+	+

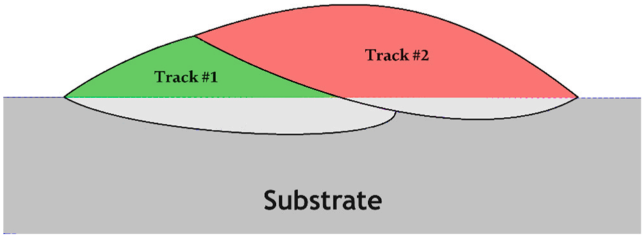

Fig. 2. Schematic illustration of the two adjacent deposited tracks used in this study for each condition.

squared pixel of 0.87 μm). Tracks were measured stitching multiple FoVs, resulting in a measured area of (6 ×4) mm. The track characterization focused on evaluating:

- the track height h, by means of height segmentation based on material ratio curve [37];
- the track width, by evaluating the width of 30 equally spaced sampled profiles across the track and reporting mean ($\overline{w}$) and standard deviation ($s(w)$);
- the discontinuity height from the top surface of the track, evaluated on the same 30 profiles and reporting the mean ($\overline{h_d}$) and the standard deviation ($s(h_d)$);
- surface topography parameters on the top surface of the track, identifying a region of interest (excluding the start or end part of the deposition) of (3.5 ×7) mm and reporting Sa, Sq, Sz, Sp and Sdq parameters on the Scale-Limited surface (obtained applying Robust Gaussian filters with nesting indexes N_{is} and N_{ic} of 0.8 μm and 0.25 mm, respectively for the S- and L-filter) [38].

Cross-sections were then extracted from the tracks, polished and etched. Different features such as dilution and porosity content were characterized by processing LOM micrographs by image analysis using ImageJ software, and the microstructure was studied by means of SEM. Moreover, the hardness measurements were carried out by using Anton Paar MCT^3 micro-instrumented indentation [39] tester (always located in metrological room of the Mind4Lab at DIGEP- Politecnico di Torino) by applying loading-holding-unloading force-controlled cycles of 30 s, 20 s and 30 s, respectively with a maximum applied force of 0.5 N by means of a Vickers indenter. The characterization was performed on the cross section to map with three parallel lines the evolution of indentation hardness (H_{IT}) across the deposited track. The map was set with a matrix of 3 × 40 indentations, with a spacing of (60 ×40) μm. The indentation platform was calibrated showing a relative expanded uncertainty of 5 % on the H_{IT} [40].

As using different sets of processing parameters can lead to deposits with different features, it was also tried to optimize the nozzle travel speed, laser power, and carrier gas flow rate in a way that the deposition exhibits the best combination of high accuracy, low surface roughness and low internal defects. The response surface analysis and process optimization were done using Minitab software [41].

Table 2
Sample numbers and their corresponding values of processing parameters used for the deposition according to the implemented face-centered central composite design.

Sample	Pattern	Nozzle Speed [mm/min]	Laser Power [W]	Carrier Gas Flow Rate [l/min]
1	− − −	400	500	4.5
2	+ − −	700	500	4.5
3	− + −	400	900	4.5
4	+ + −	700	900	4.5
5	− − +	400	500	7.5
6	+ − +	700	500	7.5
7	− + +	400	900	7.5
8	+ + +	700	900	7.5
9	− 0 0	400	700	6
10	+ 0 0	700	700	6
11	0 − 0	550	500	6
12	0 + 0	550	900	6
13	0 0 −	550	700	4.5
14	0 0 +	550	700	7.5
15	0 0 0	550	700	6

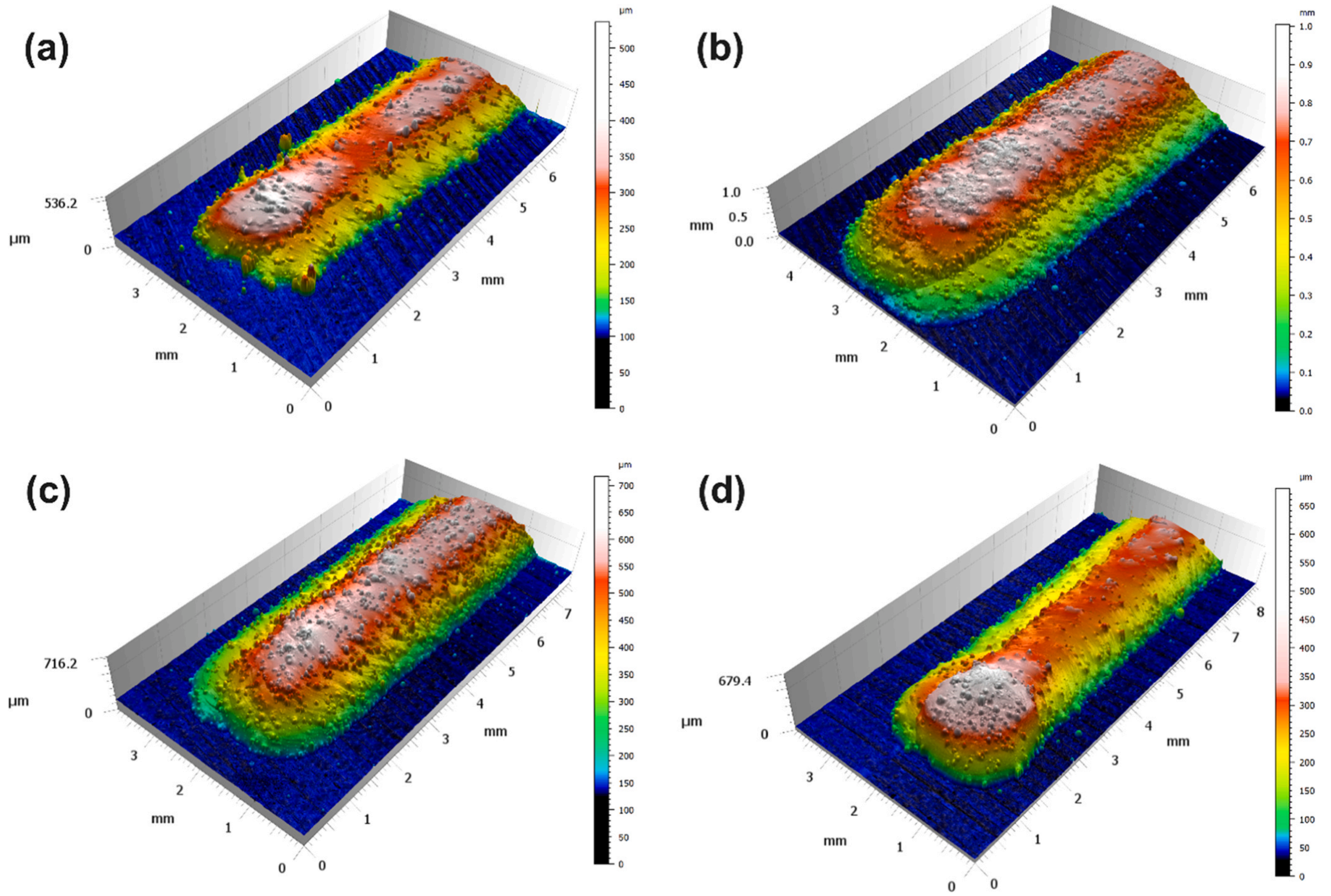

Fig. 3. 3D view and the corresponding height of samples a) #2, b) #3, c) #15, and d) #11 (see Table 2).

3. Results and discussion

3.1. *Surface topography characterization*

One of the first steps in characterizing the double tracks is to study the shape and surface properties of the deposits. The qualitative inspection showed that all depositions were continuous, and no crack or detachment was observed. Some sample results of the optical surface measurements done by CSI technique are presented in Fig. 3.

Changing the processing parameters significantly affects the shape and size of the features. As an example, by changing the nozzle speed and laser power from 700 mm/min and 500 W (sample 2) to 400 mm/min and 900 W (sample 3) both the height and width of the deposit tend to increase. This is related to the higher input energy that was used to deposit sample 3. Comparing the surface morphology at start (Fig. 3a-c) and end (Fig. 3d) points, it is evident that at the end point where the laser beam stops, there is an increase in the height of the deposit which is because of the time gap (in terms of milliseconds) between the time when nozzle reaches the end point and the laser beam stops. More in-depth details of the surface analysis, according to the methodology outlined and metrics defined in Section 2, are provided in Table 3.

Dimensional accuracy and surface roughness are the two main parameters that define the surface quality of a fabricated part. The results show that the maximum height is achieved when the laser power and

Table 3
Feature size and surface properties of the deposits.

Sample	Energy density [J/mm^2]	h [μm]	$\overline{h_d}$ [μm]	$s(h_d)$ [μm]	$\overline{w}$ [mm]	$s(w)$ [mm]	*Sa* [μm]	*Sq* [μm]	*Sdq* [-]
1	1.25	469.6	168.2	33.38	2.526	0.037	4.687	9.041	0.5831
2	0.71	266.9	52.05	32.16	2.408	0.072	3.654	6.696	0.5251
3	2.25	811.8	402.7	24.57	3.119	0.065	11.11	15.49	1.489
4	1.29	465.4	154.5	28.07	2.877	0.023	7.611	12.43	1.096
5	1.25	470.2	141.1	27.27	2.532	0.046	6.61	11.49	0.9037
6	0.71	260.5	51.44	64.51	2.412	0.076	4.345	7.792	0.5779
7	2.25	646	212.9	175.7	3.125	0.091	7.34	10.8	0.9911
8	1.29	428.1	110.7	121.1	2.909	0.037	7.63	12.64	1.04
9	1.75	597.5	122.3	84.05	2.871	0.024	9.898	13.56	1.19
10	1.00	389.9	113	110.4	2.728	0.023	6.269	10.58	0.8666
11	0.91	295.8	40.26	96.28	2.545	0.066	3.83	7.176	0.3935
12	1.64	569.5	152.7	31.25	3.011	0.091	9.781	14.55	1.258
13	1.27	446.4	93	24.09	2.821	0.063	7.755	12.11	1.33
14	1.27	483.7	95.19	29.19	2.814	0.050	9.233	13.79	1.189
15	1.27	478.6	108.5	15.48	2.802	0.035	7.025	11.08	0.9394

travel speed were at the maximum and minimum levels, respectively. Discontinuity height is defined as the difference in the height of the two adjacent tracks in each condition. Likewise, the maximum value is recorded for sample 3. With respect to the width, all tracks were supposed to be 2.8 mm in width. Therefore, samples 14 and 15, where the nozzle travel speed and laser power are not at the extremes, were among the most accurate deposits. Additionally, the width standard deviation is also a parameter which reflects the uniformity of the deposition. The lower values means that the track's width is more uniform along the deposition direction. As a result, samples 4 and 10 show the highest uniformity of the width and on the other side, samples 7 and 12 possess the highest variations of the width along the deposition. As reported in the literature, the profile of the tracks is less uniform when they are deposited with lower values of laser power [42,43].

The surface roughness of a product has a significant impact on its geometrical tolerances and is crucial for its functional and mechanical properties. It is reported that surface roughness can decrease fatigue strength to around 50 % of that of smooth surfaces [44]. The results show that the arithmetical mean height (*Sa*) value varies between 3.6 – 11.1 μm, which is lower than the values reported for DED-deposited AISI 316 L (≈15 μm) and D2 (12 – 28 μm) components [45,46]. Additionally, the root mean square height (*Sq*) and the root mean square gradient (*Sdq*) were measured to be within the range of 6.7 – 15.5 μm and 0.39 – 1.49, respectively. In a recently published work, the root mean square roughness is reported to be more than 30 μm for ASC100.29 alloy [47].

As the experiments were designed based on a systematic and efficient DoE method, the relationship between the three factors (nozzle speed v_N, laser power P, and carrier gas flow rate V_{cg}) and the morphological and topographical features of the deposits can be systematically studied. Fig. 4 depicts the effect of processing parameters on the height, width, and features of the surface roughness.

Regarding the track dimensions, it can be seen that the nozzle travel speed and laser power are the main factors affecting the width of the deposition. Decreasing the travel speed and increasing the laser power, which both increase the input energy density, result in a wider track deposition. As for the height of the tracks, similar to the tracks' width, by increasing the laser power and reducing the travel speed, which result in a higher energy density, the average height of the deposits increases. Increasing the laser power will increase the temperature of the melt pool and consequently, the melt pool width [48,49]. The layer height increases as well, which is confirmed by both experimental investigations and modeling [50,51]. Additionally, by increasing the travel speed the temperature decreases, and therefore, the width and the height of the layer tend to decrease, as observed in the results. The reduced track height at high travel speeds can be also related to the lower amount of the powder particles introduced into the melt pool [51]. In this case, the laser's effective residence time per unit of powder transferred to the melt pool declines. However, in Inconel 718 deposition it was shown that laser power does not greatly affect the deposition height [52]. This different result can be due to various reasons such as the powder catchment efficiency, power characteristics, material properties, etc. It should be noted that the volumetric or linear energy density alone cannot predict the morphology of the tracks, as there are other important causes such as physical phenomena and powder feed [53].

Results revealed the negligible effect of carrier gas flow rate (V_{cg}) on the morphological features of the deposits. However, at high V_{cg}, as the particles reach the melt pool at higher velocities, it is possible that some particles reflect from the melt pool and are not fully incorporated into it. The turbulence generated above the melt pool can lead to higher surface roughness by creating some peaks, as the results revealed. Another possible reason is that by altering the carrier gas flow rate, the convergence plane of the powder stream changes. It is shown that increasing the gas flow rate rises the convergence plane of the powder stream to distances closer to the nozzle head [54]. Therefore, while depositing with high gas flow rates, the substrate is not positioned at the focus plane of the powder stream, and consequently, more particles may reach the border of the melt pool and increase the roughness by not being fully incorporated. In line with our results, it is reported that higher values of the ratio between shielding and carrier gas flow rates led to a better surface finish and higher powder efficiencies [43].

The maximum peak height (*Sp*) is affected by the processing parameters in different ways. Increasing travel speed can significantly increase the *Sp* value of the surface. This can be because of Plateau Raleigh instability that occurs at high traveling speeds which can cause non-uniform deposition [55]. Plateau–Rayleigh instability, which describes the breakup of a liquid column into droplets due to surface tension effects [56], is likely to play a significant role at high travel speeds where the melt pool has a shorter interaction time with the incoming powder. Under these conditions, the instability can lead to non-uniform deposition and an increase in the S*p*, as the melt pool fragments before achieving a fully continuous flow. As mentioned earlier, not all the powders that transfer from the nozzle are incorporated into the melt pool. When the laser power is low, the melt pool is smaller and has a lower temperature compared to the condition where the power is high. Therefore, the possibility that the powder particles land on border transition zone or the tail of the melt pool, which have lower temperatures than the center of the melt pool and may not be in fully liquid state, increases [43,57]. In these regions, the particles may remain without being fully incorporated, and consequently lead to an increased *Sp* value. However, regarding the average roughness, better indicated by *Sa*, *Sq*, and the smoothness, i.e. *Sdq*, a different trend is observed. It can be stated that reducing the laser power or increasing the travel speed leads to lower values of *Sa, Sq* and *Sdq*. This can be attributed to the fact that lower laser power and higher travel speed (lower energy densities) lessen the intensity of thermal instabilities and melt pool convection and associated turbulence, which in turn reduces the formation of surface irregularities. On the other side, regarding the *Sz*, an initial increase is observed followed by a decrease when the travel speed increases from 400 to 700 mm/min or the laser power increases from 500 to 900 W. The same trend is observed by Piscopo et al. [16] on deposited 316 L steel samples. This opposite trend affecting parameters describing extreme values (*Sp*, *Sz*) and average roughness and smoothness (*Sa*, *Sq* and *Sdq*) indicates that although locally some particles might not be fully incorporated, leading to very high peaks, the overall surface topography improves.

The qualitative analysis reported in the main effects plot of Fig. 4, is then complemented by the ANOVA analysis carried out on the face-centered central composite to identify which factors are significantly affecting the characterization results (at a risk of error of 5 %), and by response surface methodology (RSM) to evaluate a regression model with interaction up to the second order to predict such response. The RSM is applied combined with a step-wise selection of parameters (α-to-enter and α-to-remove set at 15 %) to obtain a model with only significant terms [58]. Details of the models are reported in Table 4.

The analysis showed that the most significant parameter affecting the width and surface properties is laser power. However, travel speed is the most significant factor influencing the height. Additionally, in order to further elucidate the influence of the energy input on the deposition characteristics, the analysis of the results indicates that an increase in energy density correlates with a larger melt pool, and a tendency for non-uniform features on the deposit surface. These findings are in agreement with earlier studies [12,59] that report similar trends in the DED process.

3.2. Cross-section analysis

The cross-section areas of all the 15 deposits were studied and the micrographs taken by LOM are shown in Fig. 5.

It can be observed that different sets of processing parameters have led to different levels of dilution and porosity. Numerical information about the dilution and pores volume fraction is presented in Table 5, and

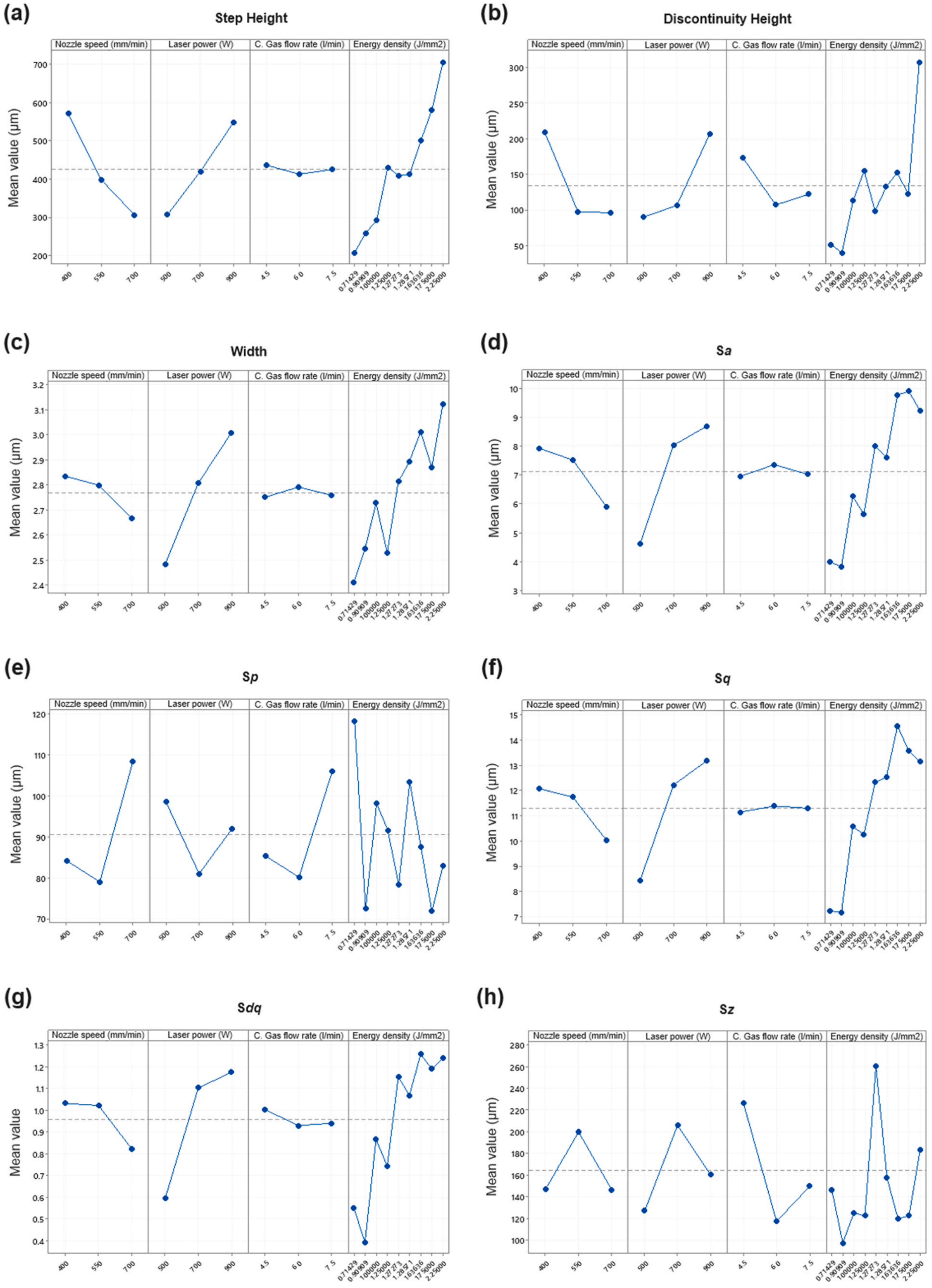

Fig. 4. The main effect of nozzle speed, laser power, and carrier gas flow rate on a) step height, b) discontinuity height, c) width average, d) arithmetic mean surface roughness (*Sa*), e) maximum peak height of the surface (*Sp*), f) the root mean square height (*Sq*), g) the root mean square gradient (*Sdq*), and h) maximum height (*Sz*). The additional variable Energy density is shown to better illustrate the combined effect of laser power and nozzle travel speed.

Table 4
Response Surface models of the geometrical and topographical characterization of the deposited tracks. Responses are in μm (but for the nondimensional parameter *Sdq*). Nozzle travel speed v_N is in mm/min, laser power P in W and the carrier gas flow rate V_{cg} in l/min. No robust model could be identified for *Sz*. Adjusted R^2 values show how well data fits the regression models.

Model Equation	R^2_{adj}
$h = 787 - 2.474v_N + 0.923P + 1.823 \times 10^{-3}v_N^2 - 5.88 \times 10^{-4}P^2$	98.12 %
$\overline{w} = 0.872 + 146 \times 10^{-3}v_N + 3.546 \times 10^{-3}P - 1 \times 10^{-6}(v_N^2 + P^2 + v_NP)$	99.27 %
$s(w) = -0.153 + 1.7 \times 10^{-3}v_N - 7.25 \times 10^{-4}P - 1.08 \times 10^{-6}v_N^2 + 7.8 \times 10^{-7}P^2 - 6.7 \times 10^{-7}v_NP$	77.60 %
$\overline{h_d} = 945 - 3.064v_N + 0.2902P - 17.3V_{cg} + 2.44 \times 10^{-3}v_N^2$	67.20 %
$s(h_d) = 100.43 - 0.289v_N + 6.69 \times 10^{-2}P - 9.51V_{cg} + 4.75 \times 10^{-4}v_N^2 - 3.34 \times 10^{-4}v_NP + 1.87 \times 10^{-2}V_{cg}P$	64.67 %
$S_q = -23.67 - 6.8 \times 10^{-3}v_N + 8.14 \times 10^{-2}P + 2.34V_{cg} - 3.53 \times 10^{-5}P^2 - 3.3 \times 10^{-3}V_{cg}P$	74.46 %
$S_p = 259.05 - 0.777v_N + 0.271P - 35.96V_{cg} + 5.82 \times 10^{-4}v_N^2 + 4.54V_{cg}^2 + 3.62 \times 10^{-2}v_NV_{cg} - 4.51 \times 10^{-2}PV_{cg}$	83.79 %
$S_a = -23.37 - 6.8 \times 10^{-3}v_N + 7.43 \times 10^{-2}P + 1.86V_{cg} - 3.44 \times 10^{-5}P^2 - 2.7 \times 10^{-3}PV_{cg}$	79.95 %
$S_{dq} = -2.15 - 7 \times 10^{-4}v_N + 1.35 \times 10^{-2}P - 0.554V_{cg} - 6.98 \times 10^{-6}P^2 + 6.87 \times 10^{-2}V_{cg}^2 - 3.86 \times 10^{-4}PV_{cg}$	81.82 %

the main effect plots are shown in Fig. 6.

It can be seen that, in general, when the energy density is lower, the dilution tends to be lower, and that the laser power is the main parameter that affects the degree of dilution. As an example, in sample 2, where the nozzle speed is at maximum and the laser power is minimum, a very low level of dilution is obtained. Analyzing Fig. 6, it is noticed that travel speed and carrier gas flow rate do not have a remarkable effect on dilution. However, altering the laser power significantly changes the dilution and by increasing the laser power from 500 to 900 W the dilution can go from about 7 % to as high as 30 %. At higher laser powers the increased temperature of the melt pool allows deeper penetration of the material [60]. The negligible reduction in the dilution by lowering the traveling speed can be attributed to the prolonged interaction time that increases the melt pool size (height and width) which accordingly reduces the energy reaching the substrate material and dilution [59]. Moreover, carrier gas flow rate was revealed to be a non-significant factor in dilution as already observed by Shin et al. [61]. Quantitative analysis performed by ANOVA and RSM, with stepwise model terms selection, resulted in predictive models reported in Table 6.

There is no specific value for dilution that can be considered as the optimum. However, in the literature, the values in the range of 10–30 % are deemed acceptable [2,26,62]. In conditions with values lower than 10 % the risk of lack of fusion (LoF) is increased, and on the other side, by having a dilution greater than 30 % keyhole pores are more likely to form [63].

The results revealed that the volume fraction of porosity ranged between 0.04 % to 1.72 %; the large dispersion results in a more limited representativeness of the model having an R^2_{adj} of 56 %. In a maraging steel samples build with different laser powers the porosity content was reported to be between 0.47 % to 1.7 % [60], thus having larger but less variable porosity. Pores in components made by DED can generally be classified into three groups: keyhole, LoF, and gas porosity. Keyholes are normally formed at high energy levels due to localized evaporation, while LoFs are generated as a result of insufficient melting and penetration at low energy densities. Additionally, the gas pores can be formed because of shielding gas entrapment in the melt pool during processing, entrapped gas in the powder particles, and evaporation of elements [3]. LoFs are normally irregular-shaped and formed between layers. Based on the results, no LoF was observed in the deposited tracks

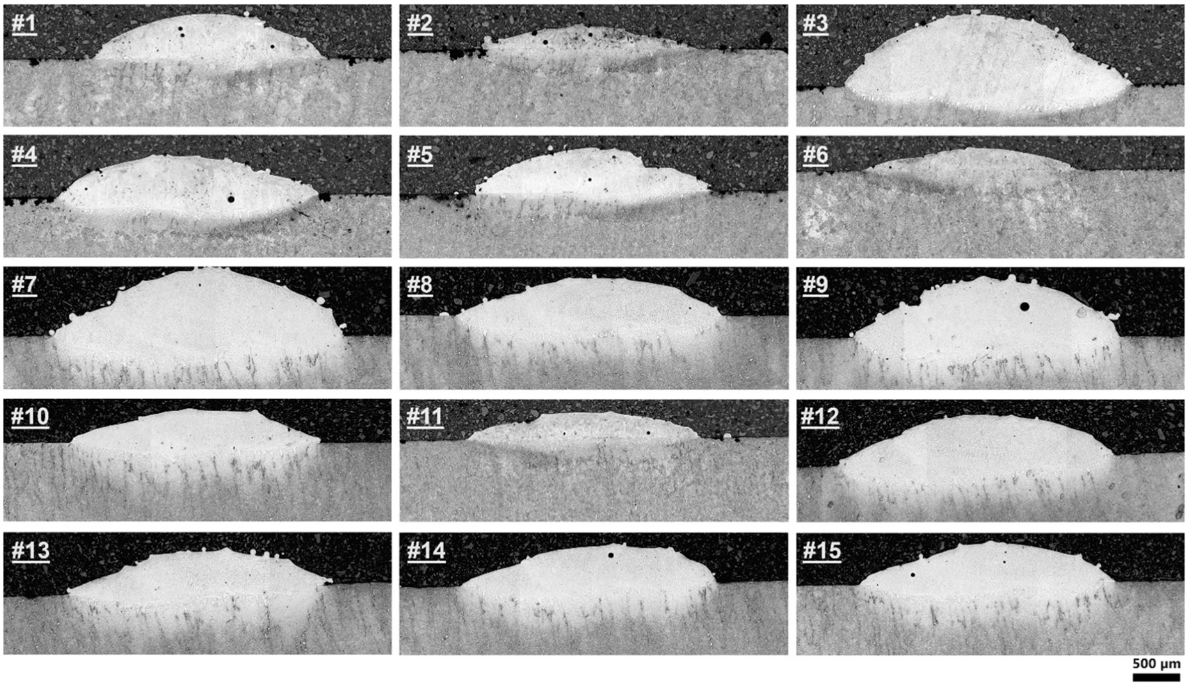

Fig. 5. LOM micrographs of cross-section areas of the deposited samples (samples numbers are shown in the images).

Table 5
Calculated values of dilution and volume fraction of pores of deposits in different samples.

Sample	1	2	3	4	5	6	7	8	9	10	11	12	13	14	15
Dilution (%)	10.48	5.34	29.14	32.91	7.75	5.28	26.14	36.16	21.39	23.92	6.40	27.02	23.34	24.88	22.56
Porosity (%)	0.69	1.72	0.42	0.70	0.44	0.47	0.07	0.06	0.70	0.25	0.42	0.04	0.10	0.27	0.32

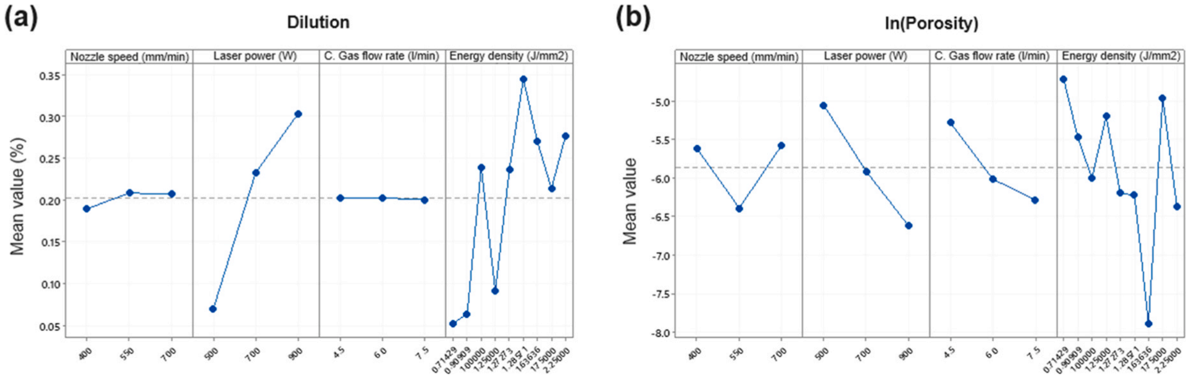

Fig. 6. The effect of the three processing parameters on a) dilution and b) porosity of the tracks. Considering the lognormality of porosity, the graph is reported for ln(p) [33].

Table 6
Response Surface models of the dilution d (in percentage) and porosity p (in percentage). Nozzle travel speed v_N is in mm/min, laser power P in W and the carrier gas flow rate V_{cg} in l/min. Considering the lognormality of porosity, the model is reported for ln(p) [33].

Model Equation	R^2_{adj}
$d = -0.04 - 2\times10^{-3}P - 0.136V_{cg} - 8.63\times10^{-4}v_N + 9\times10^{-3}V_{cg}^2 - 1.34\times10^{-6}P^2 + 8.92\times10^{-7}v_NP + 4.95\times10^{-5}v_NV_{cg}$	98.84 %
$\ln(p) = 8.95 - 3.89\times10^{-2}v_N - 3.9\times10^{-3}P - 0.335V_{cg} - 3.53\times10^{-5}v_N^2$	56.15 %

and the observed pores have a high level of circularity. By moving from high travel speeds and low laser powers (low energy densities) to low travel speeds and high powers (high energy densities) the porosity content decreases. This suggests that at higher energy densities, more entrapped gases have enough time to escape from the melt pool. However, by further lowering the travel speed the area fraction of pores increases which might be the initial step of activation of another porosity formation mechanism, such as element evaporation and keyholing [64].

Deposition angle (α) is another important factor which can affect the porosity content of multi-track and multi-layer deposits. It has been reported that the angle should be greater than 100° to avoid pores formation in overlapping tracks [65]. In this study, the α angle ranged between 124° to 158°. Thus, in all cases, the angle was more than the lower limit, and this can also be justified with the fact that no lack of fusion between the two adjacent tracks was observed in the cross-section analysis.

The LOM micrographs from Fig. 5 showed that there are different heat-affected zones (HAZ) where the microstructure of that region is different from that of both the deposited layer and the base plate. To better understand the differences, SEM micrographs were taken at high magnifications, and as can be seen in Fig. 7, they unveiled different microstructural characteristics at different locations of the samples.

The microstructure of the substrate (Fig. 7b) is characterized by tempered martensitic matrix with both spherical and elongated carbides. EDS results revealed that grey carbides are rich in Cr, V, Mo, and Mn, while bright and white spots are recognized as Nb carbide. Additionally, the micrographs (Fig. 7a and f) indicate that the deposited material has an equiaxed cellular microstructure with the presence of retained austenite and segregation of the alloying elements in the cellular boundaries. The presence of retained austenite has already been observed in different steel grades such as maraging steel [60] and hot work tool steels [66,67].

However, the microstructure of the HAZ, located between the two regions, is slightly modified compared to that of the substrate. It is characterized by lath martensite and spherical carbides, which are bigger in the region close to the unaffected substrate (Fig. 7c and d). This can be attributed to the thermal cycle affecting this region and providing microstructural coarsening. This led to the change in the martensitic microstructure and the partial dissolution of primary elongated carbides. The microstructure of the HAZ layers just below the deposited

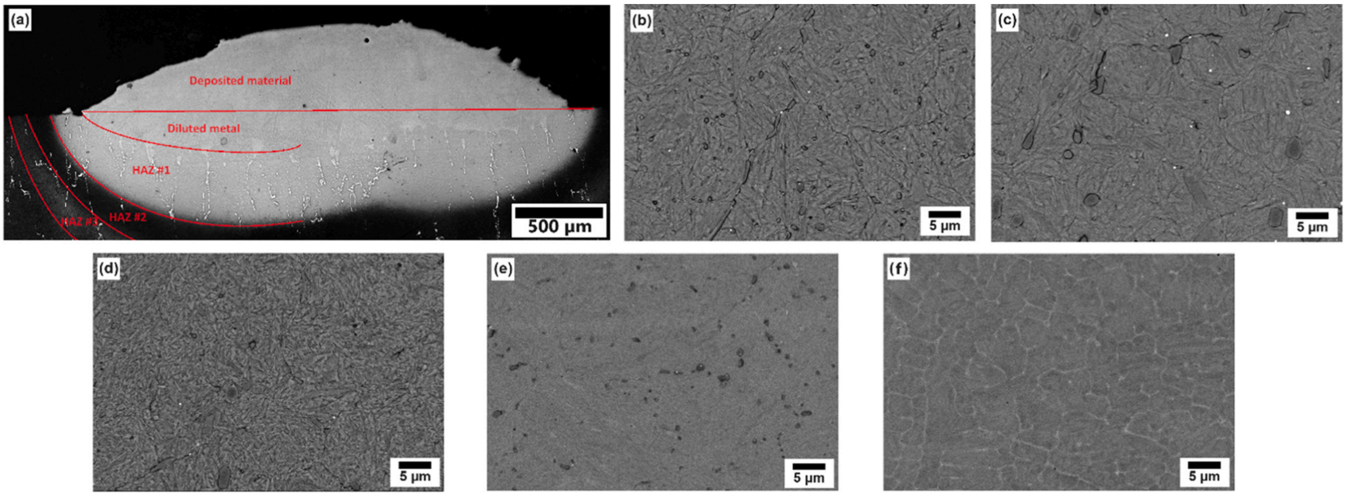

Fig. 7. a) Micrograph of the cross-section area of sample deposited with a nozzle speed of 400 mm/min, laser power of 900 W, and 4.5 l/min flow gas rate and the regions at higher magnifications: b) substrate, c) HAZ #3, d) HAZ #2, e) HAZ #1, and f) deposited material.

material (Fig. 7e) are somehow more difficult to be identified. It should be defined as a transition layer, where elongated and fine carbides are still visible, but the matrix microstructure could be a very fine quenched and smoothly tempered martensite.

The thermal history, thermal gradient, and cooling rate of a component during the fabrication process (following or overlapping deposition layers) markedly affect the final microstructure. Considering the variability of the factors and parameters affecting thermal history, predicting the microstructure becomes challenging and difficult due to the intricate relationship between thermal history and all different variables. Therefore, microstructural evolution and the effects of different processing parameters on the microstructural features will be discussed in a separate study.

3.3. Process optimization and validation

Based on the results analyzed in the previous sections, in order to obtain a deposit with the best possible surface properties (having a low surface roughness and high deposition accuracy) and the minimum possible internal defects, the processing parameters optimization was performed. In the optimization process, it was tried to keep the deposit width $\overline{w}$ close to the design target of 2.8 mm, to obtain a dilution d of around 20 % (as the mid-range value), and to minimize the porosity p, the surface properties (Sdq, Sa, Sq, discontinuity height $\overline{h_d}$), and the width dispersion, thus aiming at improving geometric precision. Process optimization is performed according to weighted and bounded parametric optimization for composite desirability, i.e. Desirability Optimization Methodology [34]. The methodology allows to optimize multiple response variables, while catering for different constraints and importance criterion. The approach allows associating with the targets two parameters, the importance, and the weight, which constraints the desirability of the solution in a neighborhood of the specified value. In particular, it should be noted that eliminating the internal defects like pores by post-processing treatments (such as hot isostatic pressing) is much more challenging, time consuming, and costly than improving the surface roughness by machining. In the case of repair by DED any postprocessing would also affect the substrate properties and this further limits the appealing of such strategy. Therefore, minimizing the pore content was given a higher weight than those others related to the surface roughness, with a ratio of 3:1, that is similar to the cost ratio of the post-processing to recover internal and external defects. Fig. 8 reports the optimization results, which, based on the calculations, identified a set of processing parameters capable of depositing tracks possessing the optimum combination of morphological and topographical features according to the requirements mentioned earlier. In other words, a deposition which is made by this set of processing parameters is expected to have the best possible combination of high geometrical accuracy and precision (in terms of mean width and its variability), low surface roughness, and low porosity fraction area. Considering the given 3:1 ratio, it can be noted that the optimized value of the laser power is around 660 W, at a nozzle travel speed of about 530 mm/min and a gas flow rate of 6.3 l/min, where the best combination of surface quality, accuracy, and internal defects can be achieved. Deviations from these optimum conditions—whether by too much laser power, too fast or too slow travel speed, or improper gas flow—tend to disrupt this balance, leading to a degradation in surface quality and dimensional accuracy. As an example, increasing laser power enhances melting and fusion, improving surface roughness up to an optimum, but excessive power can lead to irregularities and increase the variation in the width of the deposit along the track. Similarly, too low or too high nozzle speeds negatively affect the porosity content and dimensional accuracy. Meanwhile, an appropriate carrier gas flow ensures a stabilized melt pool and particle integration, whereas inadequate or excessive flow can disturb the process and affect track geometry.

To experimentally validate the calculations, six double-tracks with the rounded values of the processing parameters, nozzle travel speed of 530 mm/min, laser power of 660 W, and carrier gas flow rate of 6.3 l/min, were deposited and characterized. The predicted and real

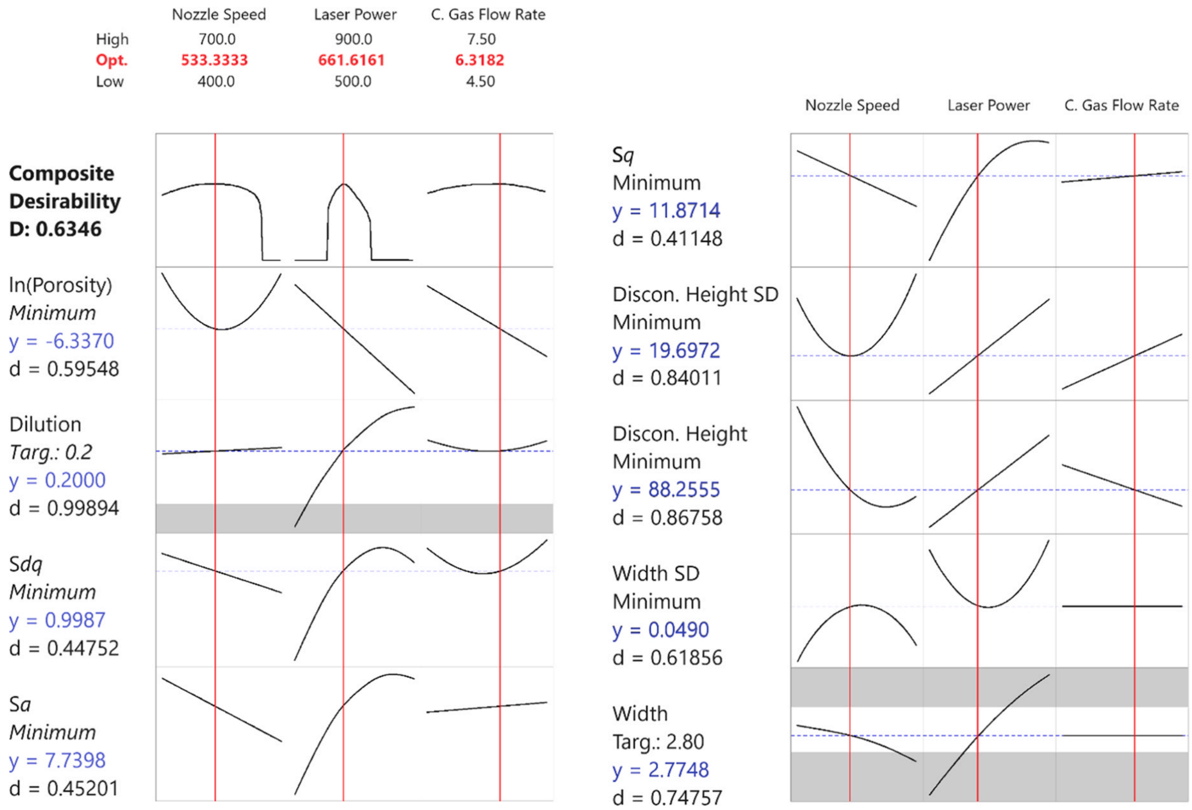

Fig. 8. Process optimization results (obtained by the software Minitab).

Table 7
The predicted and measured validation values of morphological and topographical features for the track deposited with the optimized set of processing parameters. Values report mean and uncertainty at 95 % confidence level computed as prediction interval for the model prediction and the deposition reproducibility for the experimental results. For the porosity, the mean and an asymmetrical interval is reported due to its lognormal distribution.

Feature	Porosity content (%)	Dilution (%)	w [mm]	$s(w)$ [mm]	h_d [µm]	S_{dq} [µm]	S_a [µm]	S_q [µm]
Target	Lowest possible	Close to 20 %	Close to 2.8 mm	Lowest possible	Lowest possible	Lowest possible	Lowest possible	Lowest possible
Predicted value	0.17 (0.03; 1.11)	19.85 ± 0.03	2.77 ± 0.051	0.05 ± 0.027	89.66 ± 106.2	0.997 ± 0.35	7.74 ± 2.5	11.87 ± 3.28
Experimental value	0.08 ± 0.02	23.3 ± 3.2	2.85 ± 0.03	0.03 ± 0.013	131.95 ± 203.5	1.732 ± 0.342	10.972 ± 4.08	15.973 ± 3.79

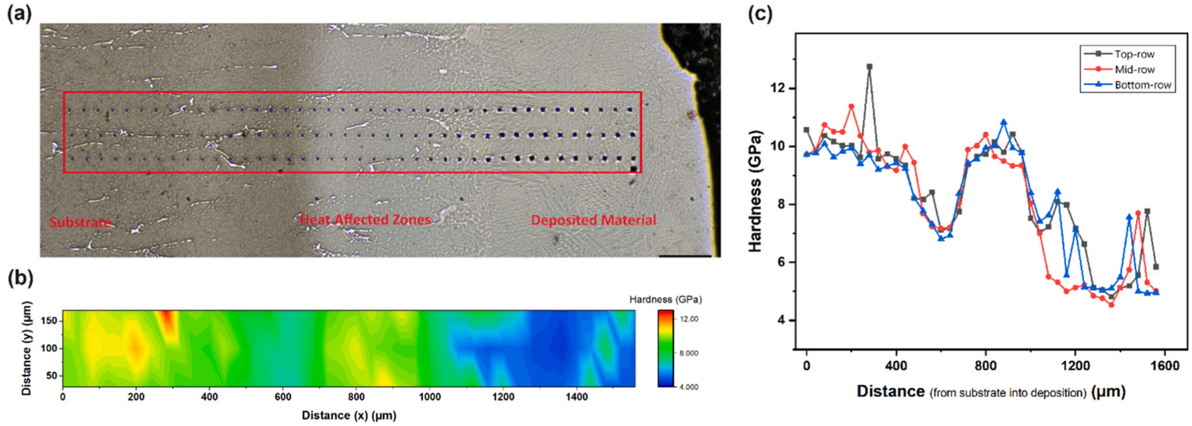

Fig. 9. a) Selected region for the microhardness indentations, b) Microhardness map of the selected region, and c) hardness profile of the selected region in GPa.

experimental values (reported as the average value of the six deposits) of the features are listed in Table 7.

To statistically validate the consistency between the predicted and the experimental values obtained in optimal process conditions, a hypothesis test was performed. Specifically, hypothesis test based on t-Student distribution for the sample average with a confidence level of 99.73 % (conventional in the Quality field) could not highlight systematic differences of the measured values obtained by optimized parameters from the predicted ones.

Micro-instrumented indentation test was conducted on an area consisting of all the deposit, HAZ, and base plate regions (Fig. 9a), to prepare a hardness map (Fig. 9b). This approach offers a clear visual representation of how the deposition process and varying microstructures influence hardness across different regions, and provides insights into the material's performance. The results, as illustrated in Fig. 9, show that there is an inner layer of about 100 µm, located between the substrate and the outer layers of the heat affected zone, where the hardness is within the range of 6.5 to 7.5 GPa. The hardness of this region is lower than those of the substrate (around 9 – 11 GPa) and the outer HAZ, exhibiting a hardness similar to that of the substrate. Additionally, the hardness of the deposition is considerably lower than that of the substrate, showing values of about 5 GPa, highlighting a clear difference from the substrate material. These findings corroborate the microstructural observations from the previous section. It is worthwhile noting that isolated hardness peaks recorded in the substrate and in the outer HAZ are associated with the location of the specific indents on large carbides. Additionally, the hardness fluctuation recorded in the HAZ layers is related to a different distribution of carbides (coarser but more dispersed) and a coarsening of the martensitic matrix (see as reference Fig. 7c, d and e). As it was observed in Fig. 7 f, the presence of unaltered solidification structures with negligible presence of carbides in the deposited material can explain the relatively soft nature of the deposited layers.

This variation in the hardness values is attributed to the applied thermal cycles and different cooling rates. The results confirm the presence of an HAZ and softer deposition, reinforcing the need for a post-process heat treatment to improve material performance, even after optimizing the processing parameters. Future studies will explore the potential benefits of heat treatment cycles to reduce these hardness variations.

4. Conclusion

In this study, the processability of K340 cold work tool steel by DED process was investigated. Based on a Design of Experiments approach, fifteen double tracks with different sets of laser power, nozzle travel speed, and carrier gas flow rate were deposited. The surface topography and cross-sections of tracks were systematically studied, and process optimization was performed by Desirability Optimization Methodology. According to the results, it can be concluded that:

1) Laser power was the most significant factor affecting the width and surface characteristics of the deposits. On the other hand, the height of the tracks was mainly influenced by the nozzle travel speed. Moreover, increasing the energy density, as a general trend, had a negative impact on surface roughness features, except *Sp*.
2) The effect of nozzle travel speed and carrier gas flow rate on the dilution was shown to be negligible. On the other hand, it varied between 5 % to 36 %, mainly affected by laser power. Near-full dense deposits were obtained using high laser powers and low travel speeds.
3) Microstructural analysis revealed the presence of different HAZ layers and deposits with a different microstructure with respect to the substrate. It was also confirmed that these regions have different hardness values.
4) Process optimization was carried out as per weighted and bounded parametric optimization for composite desirability. The predicted values for surface features, porosity, and dilution were also validated by experimental results.

The current work showed that K340 steel powder can be processed by DED technique after optimizing the processing parameters. This is highly beneficial in repairing dies and tools, which is towards sustainability in the manufacturing sector. However, in future works, microstructural homogenization by performing a post-processing heat treatment should be studied.

Declaration of Competing Interest

The authors declare that they have no known competing financial interests or personal relationships that could have appeared to influence the work reported in this paper.

References

[1] Vafadar A, Guzzomi F, Rassau A, Hayward K. Advances in metal additive manufacturing: a review of common processes, industrial applications, and current challenges. Appl Sci (Switz) 2021;11:1–33. https://doi.org/10.3390/app11031213.

[2] Ahn DG. Directed Energy Deposition (DED) process: state of the art. Int J Precis Eng Manuf - Green Technol 2021;8:703–42. https://doi.org/10.1007/s40684-020-00302-7.

[3] Svetlizky D, Das M, Zheng B, Vyatskikh AL, Bose S, Bandyopadhyay A, Schoenung JM, Lavernia EJ, Eliaz N. Directed energy deposition (DED) additive manufacturing: physical characteristics, defects, challenges and applications. Mater Today 2021;49:271–95. https://doi.org/10.1016/j.mattod.2021.03.020.

[4] Kumar SP, Elangovan S, Mohanraj R, Srihari B. Critical review of off-axial nozzle and coaxial nozzle for powder metal deposition. Mater Today Proc 2021;46:8066–79. https://doi.org/10.1016/J.MATPR.2021.03.037.

[5] Singh A, Kapil S, Das M. A comprehensive review of the methods and mechanisms for powder feedstock handling in directed energy deposition. Addit Manuf 2020;35:101388. https://doi.org/10.1016/J.ADDMA.2020.101388.

[6] Tang Z, Liu W, Wang Y, Saleheen KM, Liu Z, Peng S, Zhang Z, Zhang H. A review on in situ monitoring technology for directed energy deposition of metals. Int J Adv Manuf Technol 2020;108:3437–63. https://doi.org/10.1007/s00170-020-05569-3.

[7] Svetlizky D, Zheng B, Vyatskikh A, Das M, Bose S, Bandyopadhyay A, Schoenung JM, Lavernia EJ, Eliaz N. Laser-based directed energy deposition (DED-LB) of advanced materials. Mater Sci Eng: A 2022;840:142967. https://doi.org/10.1016/J.MSEA.2022.142967.

[8] Naebe M, Shirvanimoghaddam K. Functionally graded materials: a review of fabrication and properties. Appl Mater Today 2016;5:223–45. https://doi.org/10.1016/J.APMT.2016.10.001.

[9] Pratheesh Kumar S, Elangovan S, Mohanraj R, Ramakrishna JR. A review on properties of Inconel 625 and Inconel 718 fabricated using direct energy deposition. Mater Today Proc 2021;46:7892–906. https://doi.org/10.1016/J.MATPR.2021.02.566.

[10] Sibisi PN, Popoola API, Arthur NKK, Pityana SL. Review on direct metal laser deposition manufacturing technology for the Ti-6Al-4V alloy. Int J Adv Manuf Technol 2020;107:1163–78. https://doi.org/10.1007/s00170-019-04851-3.

[11] Pinkerton AJ. Advances in the modeling of laser direct metal deposition. J Laser Appl 2014;27:S15001. https://doi.org/10.2351/1.4815992.

[12] Chen B, Huang Y, Gu T, Tan C, Feng J. Investigation on the process and microstructure evolution during direct laser metal deposition of 18Ni300. Rapid Prototyp J 2018;24:964–72. https://doi.org/10.1108/RPJ-01-2018-0022.

[13] Eo DR, Park SH, Cho JW. Controlling inclusion evolution behavior by adjusting flow rate of shielding gas during direct energy deposition of AISI 316 L. Addit Manuf 2020;33. https://doi.org/10.1016/j.addma.2020.101119.

[14] Nagulin KY, Iskhakov FR, Shpilev AI, Gilmutdinov AK. Optical diagnostics and optimization of the gas-powder flow in the nozzles for laser cladding. Opt Laser Technol 2018;108:310–20. https://doi.org/10.1016/J.OPTLASTEC.2018.07.001.

[15] J.E. Smugeresky, D.M. Keicher, J.A. Romero, M.L. Griffith, L.D. Harwell, Laser engineered net shaping (LENS{trademark}) process: Optimization of surface finish and microstructural properties, in: 1997. ⟨https://api.semanticscholar.org/CorpusID:136703564⟩.

[16] Piscopo G, Salmi A, Atzeni E. Influence of high-productivity process parameters on the surface quality and residual stress state of AISI 316L components produced by directed energy deposition. J Mater Eng Perform 2021;30:6691–702. https://doi.org/10.1007/s11665-021-05954-3.

[17] Rombouts M, Maes G, Hendrix W, Delarbre E, Motmans F. Surface finish after laser metal deposition. Phys Procedia 2013;41:810–4. https://doi.org/10.1016/J.PHPRO.2013.03.152.

[18] Cao L, Li J, Hu J, Liu H, Wu Y, Zhou Q. Optimization of surface roughness and dimensional accuracy in LPBF additive manufacturing. Opt Laser Technol 2021;142:107246. https://doi.org/10.1016/J.OPTLASTEC.2021.107246.

[19] K. Böhler, COLD WORK TOOL STEEL, n.d. ⟨https://www.bohler-edelstahl.com/app/uploads/sites/92/2020/07/productdb/api/k340en_isodur.pdf⟩ (accessed September 12, 2023).

[20] Simoneau L, Bois-Brochu A, Blais C. Tensile properties of built and rebuilt/repaired specimens of 316L stainless steel using directed energy deposition. J Mater Eng Perform 2020;29:6139–46. https://doi.org/10.1007/s11665-020-05087-z.

[21] Rauch Matthieu, Hascoët Jean-Yves, Mallaiah Manjaiah. Repairing Ti-6Al-4V aeronautical components with DED additive manufacturing. MATEC Web Conf 2020;321:3017. https://doi.org/10.1051/matecconf/202032103017.

[22] Wilson JM, Piya C, Shin YC, Zhao F, Ramani K. Remanufacturing of turbine blades by laser direct deposition with its energy and environmental impact analysis. J Clean Prod 2014;80:170–8. https://doi.org/10.1016/J.JCLEPRO.2014.05.084.

[23] Narvan M, Al-Rubaie KS, Elbestawi M. Process-structure-property relationships of AISI H13 tool steel processed with selective laser melting. Materials 2019;12. https://doi.org/10.3390/ma12142284.

[24] Krell J, Röttger A, Geenen K, Theisen W. General investigations on processing tool steel X40CrMoV5-1 with selective laser melting. J Mater Process Technol 2018;255:679–88. https://doi.org/10.1016/j.jmatprotec.2018.01.012.

[25] Shrestha S, Chou K. A study of transient and steady-state regions from single-track deposition in laser powder bed fusion. J Manuf Process 2021;61:226–35. https://doi.org/10.1016/J.JMAPRO.2020.11.023.

[26] Morales C, Merlin M, Fortini A, Fortunato A. Direct energy depositions of a 17-4 PH stainless steel: geometrical and microstructural characterizations. Coatings 2023;13. https://doi.org/10.3390/coatings13030636.

[27] Weissman SA, Anderson NG. Design of Experiments (DoE) and process optimization. A review of recent publications. Org Process Res Dev 2015;19:1605–33. https://doi.org/10.1021/op500169m.

[28] Ng GKL, Jarfors AEW, Bi G, Zheng HY. Porosity formation and gas bubble retention in laser metal deposition. Appl Phys A 2009;97:641–9. https://doi.org/10.1007/s00339-009-5266-3.

[29] Sheshadri R, Nagaraj M, Lakshmikanthan A, Chandrashekarappa MPG, Pimenov DY, Giasin K, Prasad RVS, Wojciechowski S. Experimental investigation of selective laser melting parameters for higher surface quality and microhardness properties: taguchi and super ranking concept approaches. J Mater Res Technol 2021;14:2586–600. https://doi.org/10.1016/J.JMRT.2021.07.144.

[30] Lian G, Zhang H, Zhang Y, Tanaka ML, Chen C, Jiang J. Optimizing processing parameters for multi-track laser cladding utilizing multi-response grey relational analysis. Coatings 2019;9. https://doi.org/10.3390/coatings9060356.

[31] Galetto M, Genta G, Maculotti G, Verna E. Defect probability estimation for hardness-optimised parts by selective laser melting. Int J Precis Eng Manuf 2020;21:1739–53. https://doi.org/10.1007/s12541-020-00381-1.

[32] Maculotti G, Genta G, Galetto M. Optimisation of laser welding of deep drawing steel for automotive applications by Machine Learning: a comparison of different techniques. Qual Reliab Eng Int 2024;40:202–19. https://doi.org/10.1002/qre.3377.

[33] Ghibaudo C, Maculotti G, Gobber F, Saboori A, Galetto M, Biamino S, Ugues D. Information-rich quality controls prediction model based on non-destructive analysis for porosity determination of AISI H13 produced by electron beam melting. Int J Adv Manuf Technol 2023;126:1159–73. https://doi.org/10.1007/s00170-023-11153-2.

[34] Derringer G. A balancing act: optimizing a product's properties. Qual Prog 1994. ⟨https://api.semanticscholar.org/CorpusID:64404412⟩.

[35] Svetlizky D, Zheng B, Steinberg DM, Schoenung JM, Lavernia EJ, Eliaz N. The influence of laser directed energy deposition (DED) processing parameters for Al5083 studied by central composite design. J Mater Res Technol 2022;17:3157–71. https://doi.org/10.1016/J.JMRT.2022.02.042.

[36] Montgomery DC. Design and analysis of experiments. 8th ed.,. John Wiley & Sons,; 2012.

[37] Maculotti G, Goti E, Genta G, Mazza L, Galetto M. Uncertainty-based comparison of conventional and surface topography-based methods for wear volume evaluation in pin-on-disc tribological test. Tribol Int 2022;165:107260. https://doi.org/10.1016/J.TRIBOINT.2021.107260.

[38] BS EN ISO 25178–2:2022, Geometrical product specifications (GPS). Surface texture: Areal Terms, definitions and surface texture parameters, 2022.

[39] ISO 14577–1:2015, Instrumented indentation test for hardness and materials parameters. Part 1: Test method, 2015.

[40] Galetto M, Genta G, Maculotti G. Single-step calibration method for nano indentation testing machines. CIRP Ann 2020;69:429–32. https://doi.org/10.1016/J.CIRP.2020.03.015.

[41] Minitab L.L.C., Minitab, Available from: ⟨Https://Www.Minitab.Com/En-Us/⟩ (n.d.).

[42] Peyre P, Gharbi M, Gorny C, Carin M, Morville S, Carron D, Le Masson P, Malot T, Fabbro R. Surface finish issues after direct metal deposition. Mater Sci Forum 2012;706–709:228–33. https://doi.org/10.4028/www.scientific.net/MSF.706-709.228.

[43] Jardon Z, Ertveldt J, Lecluyse R, Hinderdael M, Pyl L. Directed energy deposition roughness mitigation through laser remelting. Procedia CIRP 2022;111:180–4. https://doi.org/10.1016/J.PROCIR.2022.08.042.

[44] J.H. Ryu, S.W. Nam, Effect of surface roughness on low-cycle fatigue life of Cr-Mo-V steel at 550 °C, 1989.

[45] Moheimani SK, Iuliano L, Saboori A. The role of substrate preheating on the microstructure, roughness, and mechanical performance of AISI 316L produced by directed energy deposition additive manufacturing. Int J Adv Manuf Technol 2022;119:7159–74. https://doi.org/10.1007/s00170-021-08564-4.

[46] Omar SMT, Plucknett KP. Influence of layer thickness upon the dimensional accuracy and surface roughness of AISI D2 tool steel manufactured using directed energy deposition. In: Proceedings of the 61st conference of metallurgists, COM 2022. Cham: Springer International Publishing; 2023. p. 39–42.

[47] dos Santos Paes LE, Pereira M, Xavier FA, Weingaertner WL, D'Oliveira ASCM, Costa EC, Vilarinho LO, Scotti A. Understanding the behavior of laser surface remelting after directed energy deposition additive manufacturing through comparing the use of iron and Inconel powders. J Manuf Process 2021;70:494–507. https://doi.org/10.1016/J.JMAPRO.2021.08.061.

[48] Hua T, Jing C, Xin L, Fengying Z, Weidong H. Research on molten pool temperature in the process of laser rapid forming. J Mater Process Technol 2008;198:454–62. https://doi.org/10.1016/J.JMATPROTEC.2007.06.090.

[49] Peyre P, Aubry P, Fabbro R, Neveu R, Longuet A. Analytical and numerical modelling of the direct metal deposition laser process. J Phys D Appl Phys 2008;41:025403. https://doi.org/10.1088/0022-3727/41/2/025403.

[50] Pinkerton Andrew J, Li Lin. Modelling the geometry of a moving laser melt pool and deposition track via energy and mass balances. J Phys D Appl Phys 2004;37:1885. https://doi.org/10.1088/0022-3727/37/14/003.

[51] Shim DS, Baek GY, Seo JS, Shin GY, Kim KP, Lee KY. Effect of layer thickness setting on deposition characteristics in direct energy deposition (DED) process. Opt Laser Technol 2016;86:69–78. https://doi.org/10.1016/J.OPTLASTEC.2016.07.001.

[52] Lee Y, Nordin M, Babu S, Farson D. Influence of fluid convection on weld pool formation in laser cladding. Weld J 2014;93:292s–300s.

[53] Kiani P, Dupuy AD, Ma K, Schoenung JM. Directed energy deposition of AlSi10Mg: single track nonscalability and bulk properties. Mater Des 2020;194. https://doi.org/10.1016/j.matdes.2020.108847.

[54] Ferreira E, Dal M, Colin C, Marion G, Gorny C, Courapied D, Guy J, Peyre P. Experimental and numerical analysis of gas/powder flow for different LMD nozzles. Met (Basel) 2020;10. https://doi.org/10.3390/met10050667.

[55] DebRoy T, Wei HL, Zuback JS, Mukherjee T, Elmer JW, Milewski JO, Beese AM, Wilson-Heid A, De A, Zhang W. Additive manufacturing of metallic components – process, structure and properties. Prog Mater Sci 2018;92:112–224. https://doi.org/10.1016/j.pmatsci.2017.10.001.

[56] Ding X, Liu DD, Xu YM, Ding XT, Yang J, Ma ZJ. Utilizing the plateau-rayleigh instability with heat-driven nano-biosensing systems. SLAS Technol 2015;20:463–70. https://doi.org/10.1177/2211068215575688.

[57] Peyre P, Gharbi M, Gorny C, Carin M, Morville S, Carron D, Le Masson P, Malot T, Fabbro R. Surface finish issues after direct metal deposition. In: Materials Science Forum. Trans Tech Publications Ltd; 2012. p. 228–33. https://doi.org/10.4028/www.scientific.net/MSF.706-709.228.

[58] Galetto M, Genta G, Maculotti G, Verna E. Defect probability estimation for hardness-optimised parts by selective laser melting. Int J Precis Eng Manuf 2020;21:1739–53. https://doi.org/10.1007/s12541-020-00381-1.

[59] Fathi A, Toyserkani E, Khajepour A, Durali M. Prediction of melt pool depth and dilution in laser powder deposition. J Phys D Appl Phys 2006;39:2613. https://doi.org/10.1088/0022-3727/39/12/022.

[60] Félix-Martínez C, Ibarra-Medina J, Fernández-Benavides DA, Cáceres-Díaz LA, Alvarado-Orozco JM. Effect of the parametric optimization and heat-treatment on the 18Ni-300 maraging steel microstructural properties manufactured by directed energy deposition. Int J Adv Manuf Technol 2021;115:3999–4020. https://doi.org/10.1007/s00170-021-07320-y.

[61] Shin S, Kwon S-M, Kim C, Lee J, Hwang J, KIm H. Optimization of direct energy deposition of 304L stainless steel through laser process parameters. J Weld Join 2021;39:182–8. https://doi.org/10.5781/jwj.2021.39.2.7.

[62] A. Dass, Fundamentals of Solidification in Directed Energy Deposition Type Additive Manufacturing of Inconel 625, 2020. https://doi.org/https://doi.org/10.7298/f59s-yn90.

[63] Silvestri AT, Bosetti P, Squillace A. Laser-directed energy deposition of H13: processing window and improved characterization procedures. Mater Manuf Process 2023;38:1770–84. https://doi.org/10.1080/10426914.2023.2219302.

[64] L. Badi, Effect of Process Parameters on the Quality of 17–4 PH Samples Produced by Directed Energy Deposition, Politecnico di Torino, 2021. ⟨http://webthesis.biblio.polito.it/id/eprint/18461⟩.

[65] Costa L, Felde I, Réti T, Kálazi Z, Colaço R, Vilar R, Verő B. A simplified semi-empirical method to select the processing parameters for laser clad coatings. Mater Sci Forum 2002;414–415:385–94. https://doi.org/10.4028/www.scientific.net/MSF.414-415.385.

[66] Holzweissig MJ, Taube A, Brenne F, Schaper M, Niendorf T. Microstructural characterization and mechanical performance of hot work tool steel processed by selective laser melting. Metall Mater Trans B 2015;46:545–9. https://doi.org/10.1007/s11663-014-0267-9.

[67] Vinčić J, Aversa A, Lombardi M, Manfredi D. Processability and microstructural evolution of W360 hot work tool steel by directed energy deposition. Met Mater Int 2023. https://doi.org/10.1007/s12540-023-01508-5.